MATERIALS PHYSICS AND MECHANICS RESEARCH ARTICLE

Submitted: March 21, 2026 **Revised: April 29, 2026** **Accepted: May 20, 2026**

Influence of aging in B2-austenite phase on stress-induced martensitic transformation for $[001]_{B2}$-oriented $Co_{35}Ni_{35}Al_{28}Fe_2$ single crystals

A.S. Eftifeeva ✉, E.Y. Panchenko, I.D. Fatkullin, M.V. Zherdeva, V.G. Ryzhakova, Y.I. Chumlyakov

National Research Tomsk State University, Tomsk, Russia

✉ anna_eftifeeva@rambler.ru

ABSTRACT

The effect of aging in the high-temperature B2-phase on the martensitic transformation, the strength properties of $L1_0$-martensite, and the cyclic stability of superelasticity in compression in $[001]_{B2}$-oriented $Co_{35}Ni_{35}Al_{28}Fe_2$ single crystals was investigated. The B2-phase in quenched $Co_{35}Ni_{35}Al_{28}Fe_2$ single crystals remains stable without precipitation of secondary phases upon heating up to 520 K, which represents an increase of approximately 50 K compared to ternary $Co_{35}Ni_{35}Al_{30}$ alloys. Aging at 673 K leads to the precipitation of nanosized $(Ni,Co)_5Al_3$-particles providing dispersion strengthening. Short-term aging for 15 min decreases the start B2-$L1_0$ martensitic transformation temperature M_s by 140 K and significantly improves functional properties, resulting in a wide temperature range of superelasticity (345 K) and high strength properties of $L1_0$-martensite (> 1870 MPa) while maintaining cyclic stability of superelasticity.

KEYWORDS

single crystals • martensitic transformation • aging • strengthening • particles • superelasticity • yield stress

Funding. *The study was supported by the Russian Science Foundation grant No. 23–79–10093, https://rscf.ru/en/project/23–79–10093/*

Acknowledgements. *Electron microscopy studies were carried out on the equipment of the Krasnoyarsk Regional Center for Collective Use of the FRC KSC SB RA.*

Citation: Eftifeeva AS, Panchenko EY, Fatkullin ID, Zherdeva MV, Ryzhakova VG, Chumlyakov YI. Influence of aging in B2-austenite phase on stress-induced martensitic transformation for $[001]_{B2}$-oriented $Co_{35}Ni_{35}Al_{28}Fe_2$ single crystals. *Materials Physics and Mechanics*. 2026;54(3): 20–31. http://dx.doi.org/10.18149/MPM.5432026_2

Introduction

Co-Ni-Al-based alloys belong to the class of ferromagnetic shape memory alloys (FSMAs), in which the functional properties are determined by the features of the B2-$L1_0$ martensitic transformation (MT) [1,2]. The two-phase (B2+γ)-alloys exhibit high strength and ductility due to the presence of a ductile γ-phase with the FCC structure.

A number of studies on Ni-Al-, Ni-Al-Fe-, and Ni-Al-Co-based alloys have shown that the supersaturated B2-phase becomes thermally unstable at temperatures above 473 K [1,3–16]. Depending on the chemical composition and annealing temperature, in addition to the γ-phase, precipitation of several types has been reported including γ′($L1_2$), ε- and α-Co phases, as well as superstructures of the A_2B and A_5B_3 types [1,3–17]. Depending on their size, distribution and coherence with the B2-matrix, these particles can suppress the transformation, strengthen the material, reduce the MT temperatures, expand

© A.S. Eftifeeva, E.Y. Panchenko, I.D. Fatkullin, M.V. Zherdeva, V.G. Ryzhakova, Yu.I. Chumlyakov, 2026.
Publisher: Peter the Great St. Petersburg Polytechnic University
This is an open access article under the CC BY-NC 4.0 license (https://creativecommons.org/li-censes/by-nc/4.0/)

the temperature range of stress-induced MT, increase the cyclic stability of functional properties, and induce a two-way shape memory effect. Thus, the control of precipitation in Co-Ni-Al-based alloys is necessary to ensure stable material performance and obtain improved functional properties. Despite the significant progress in understanding the role of precipitation on the thermally-induced and stress-induced MT in ternary Co-Ni-Al alloys [18,19], the influence of precipitation on the functional properties during the stress-induced B2-$L1_0$ MT in Fe-alloyed Co-Ni-Al alloys remains unexplored.

Quaternary Co-Ni-Al-Fe alloys are of interest because the Fe addition of ~ 2 at. % simultaneously reduces the MT temperature and increases the Curie temperature, thereby expanding the FSMAs application. However, the Fe alloying above 3 at. % suppresses or significantly diffuses the MT, resulting in reduced reversibility [20,21]. In addition to being an effective tool for controlling the interrelated magnetic and martensitic transformations in Co-Ni-Al alloys, Fe alloying of 2 at. % should contribute to the increased thermal stability of the B2-phase.

The practical application of SMAs (damping systems and actuators) relies on the superelasticity (SE) and shape memory effect (SME) associated with stress-induced MT, which requires a systematic approach for SMAs studying. However, the influence of precipitation on stress-induced MT and the strength properties of $L1_0$-martensite in quaternary $Co_{35}Ni_{35}Al_{28}Fe_2$ alloys is still unclear. Low Fe-alloyed Co-Ni-Al-Fe alloys are expected to combine MT with improved strength and functional properties through precipitation processes during aging. Therefore, the aim of the present work is to investigate the effect of aging in the B2-phase on the stress-induced B2-$L1_0$ MT, the strength properties of $L1_0$-martensite, and the cyclic stability of SE in single crystals of the $Co_{35}Ni_{35}Al_{28}Fe_2$ alloy in compression along the $[001]_{B2}$-direction.

Materials and Methods

Single crystals of the ferromagnetic $Co_{35}Ni_{35}Al_{28}Fe_2$ (at. %) alloy were grown using the Bridgman method. The crystallographic orientation of the single crystals was determined using a X-ray diffractometer DRON-3 with $Fe_{K\alpha}$ radiation. The deviation from the exact orientation did not exceed 3°. The chemical composition and surface morphology were examined using a scanning electron microscope TESCAN VEGA 3. The samples were cut from the single-crystal ingots using a wire electrical discharge machine Arta 153.

The samples were homogenized at 1623 K for 6.0 h followed by water quenching. Isothermal aging at 673 K was carried out in a high-temperature tube furnace Carbolite. Metallographic observations were performed using a digital measuring microscope Keyence VHX-2000. The sample surfaces were mechanically ground using a grinding machine MoPao 260E and subsequently electrolytically polished in a solution.

The MT temperatures were determined from the temperature dependence of electrical resistivity. Caloric effects during cooling/heating were measured using a differential scanning calorimeter (DSC) DSC 404 F1. Compression tests were carried out using an electromechanical testing machine Instron VHS 5969. Cuboidal samples ($3.0 \times 3.0 \times 6.0$ mm^3) had the compression axis oriented along the $[001]_{B2}$-direction. The loading and unloading rate was $\dot{\varepsilon} = 10^{-3}$1/c.

The microstructure was studied using a transmission electron microscope (TEM) Hitachi HT-7700 operated at an accelerating voltage of 110 kV. Thin foils with a diameter of 3 mm and a thickness of 0.1 mm were prepared by electrolytic polishing in a solution of 20 % H_2SO_4+80 % CH_3OH at a temperature of 283 K and a voltage of 15–17 V using a twin-jet polisher Tenupol-5.

Results and Discussion

Thermal-induced martensitic transformation and thermal stability of B2-phase

The quenched single crystals exhibit a two-phase microstructure. It consists of an austenitic B2-matrix and a secondary γ-phase. The γ-phase particles have a size of ⩾ 100 μm, while their volume fraction in the B2-matrix is less than 10% (Fig. 1(a)). This phase is enriched in cobalt and depleted in aluminum compared with the matrix and does not undergo the B2-$L1_0$ MT [22]. Figure 1(b) shows a TEM image of the interphase boundary between the B2-phase with a BCC lattice and the secondary γ-phase with an FCC lattice. The selected area electron diffraction pattern (SAEDP) from the secondary phase contains superlattice reflections of the (100) and (011) types corresponding to $L1_2$ ordering (Fig. 1(c)). Thus, according to TEM analysis, the secondary γ-phase has the FCC structure (dark regions in Fig. 1(c)) containing dispersed coherent γ′($L1_2$)-particles (bright

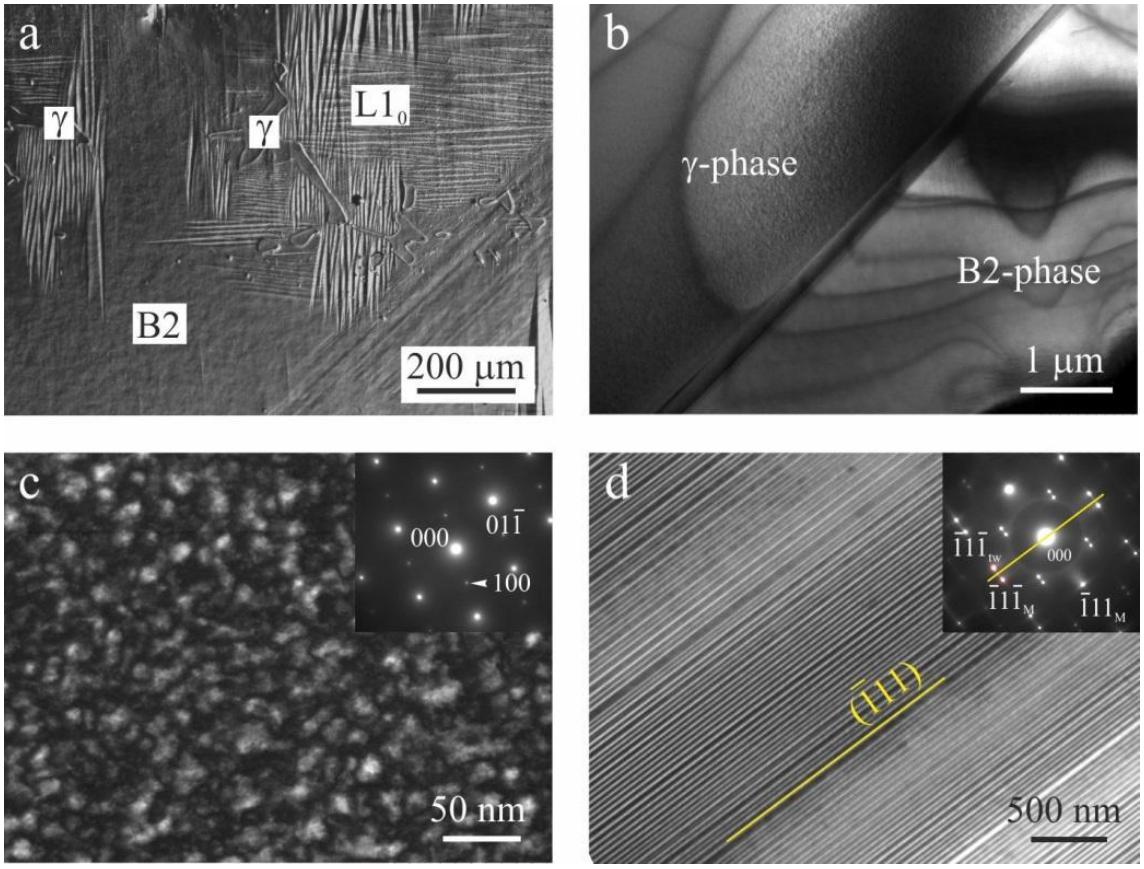


Fig. 1. Microstructure of quenched $Co_{35}Ni_{35}Al_{28}Fe_2$ single crystals: (a) optical micrograph of the surface; (b) bright-field image of the interphase B2-γ/γ′ boundary; (c) dark-field image taken using the superlattice $(100)_{FCC}$ reflection from nanosized γ′-particles and the SAEDP (zone axis $[011]_{FCC}$); (d) bright-field image of $(\bar{1}11)_{L10}$ $L1_0$-martensite twins and the SAEDP (zone axis $[110]_M||[\bar{1}\bar{1}0]_M$)

regions in Fig. 1(c)). The size of the γ′-particles varies from 3 to 10 nm, and their volume fraction in the γ-matrix reaches 25–35 %. It is known that the lattice mismatch between FCC and $L1_2$ structures is small, which results in a high degree of coherency between them [23,24]. Figure 1(d) shows $(\bar{1}11)_{L10}$ martensitic twins with a thickness of about 10–20 nm.

Figure 2(a) shows $\rho(T)$ curves. In the quenched single crystals, the forward MT starts at M_s = 270 K, while the reverse transformation starts at A_s = 235 K (Fig. 2(a), Table 1). The $\rho(T)$ curve during cooling/heating exhibits a nearly symmetric shape. The temperature intervals of the forward and reverse transformations are close in magnitude and equal to $\Delta_1 \approx \Delta_2$ = 55–60 K. The thermal-induced MT is accompanied by narrow hysteresis ΔT = 22.5 K. MT occurs at a temperature ratio of $A_s < M_s$ and, accordingly, is accompanied by the accumulation of significant elastic energy. This is associated with the elastic lattice mismatch between austenite and martensite, as well as with the interaction of martensitic variants with each other. As a result, part of the transformation free energy is stored in the form of elastic strain energy and interfacial energy, which modifies the thermodynamic balance between the phases and promotes reverse MT. A high level of stored elastic energy is one of the key factors enabling SE and stable reversibility of the MT in SMAs.

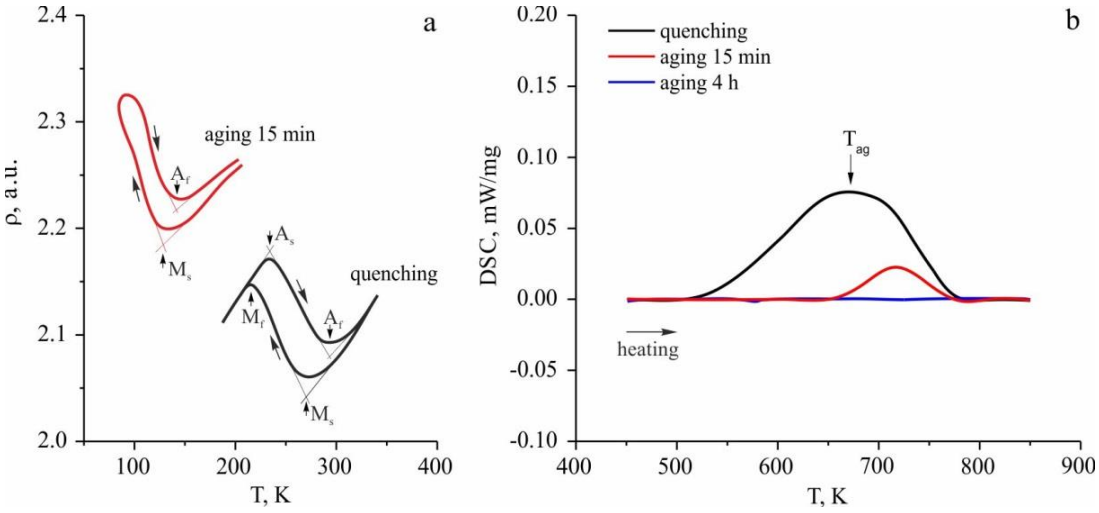


Fig. 2. Study of the MT temperatures for $Co_{35}Ni_{35}Al_{28}Fe_2$ single crystals: (a) $\rho(T)$ curves during cooling/heating (a); DSC exothermic curves during heating

Table 1. The B2-$L1_0$ MT temperatures for $Co_{35}Ni_{35}Al_{28}Fe_2$ single crystals.

Single crystals	M_s, K	M_f, K	A_s, K	A_f, K	*Δ_1, K	*Δ_2, K	*ΔT, K
Quenching	270	215	235	295	55	60	22,5
Aging 673 K, 15 min	130	< 85	< 97	137	> 45	> 40	~ 9.5
*$\Delta_1=M_s-M_f$; $\Delta_2=A_f-A_s$ $\Delta T=(A_s+A_f)/2-(M_s+M_f)/2$							

DSC curves were analyzed during cooling down to 123 K and heating up to 1173 K. The cooling and heating rate was 20 K/min. Endothermic and exothermic peaks associated with the MT are almost not observed in the DSC curves. This behavior may occur because the MT proceeds over a wide temperature interval with a low thermal effect, while electrical resistivity is more sensitive to changes in crystal structure and lattice symmetry.

On the DSC heating curve for the quenched single crystals, a pronounced exothermic peak is observed above the MT temperatures in the range from 520 to 775 K (Fig. 2(b)). No similar effect is observed during cooling, which indicates the irreversible nature of this process. Since the peak appears significantly higher than the MT temperatures (approximately A_f+225 K), it may be associated with the diffusion decomposition of the supersaturated B2-phase, i.e., the precipitation of ordered particles or the additional austenite ordering. For Ni-Al- and Co-Ni-Al-based alloys, diffusion decomposition in the B2-austenite region above about 723 K is commonly attributed to the thermodynamic instability of the B2-phase and the formation of ordered superstructures such as $(Ni,Co)_2Al$ or $(Ni,Co)_5Al_3$ [7–15].

To analyze the nature of the thermal instability of the B2-phase, the quenched single crystals were subjected to isothermal aging in austenite at 673 K, corresponding to the maximum of the DSC peak. After the aging for 15 min, the measurements of the temperature dependence of electrical resistivity showed that the M_s temperature decreased by 140 K and the A_f temperature decreased by 158 K compared to the quenched state (Fig. 2(a), Table 1). Determination of the M_f and A_s temperatures after the aging for 15 min was complicated due to their shift below 100 K, so the calculation of ΔT, Δ_1, and Δ_2 is approximate. The thermal hysteresis was ΔT = 9.5 K for aged for 15 min single crystals, which is two times lower than in the quenched single crystals. The temperature ratio of $A_s < M_s$ remains after aging for 15 min. After aging for 1 h or more, no hysteresis loop is observed in $\rho(T)$ curves. This indicates either a shift of the MT temperatures below the liquid nitrogen temperature or a suppression of the thermal-induced MT.

A change of the exothermic DSC peak is observed after aging (Fig. 2(b)). In the DSC heating curve, a less pronounced peak remains in the range of 660–765 K, indicating partial diffusion decomposition already occurring during the preliminary aging for 15 min. Relative to the A_f temperature of the quenched state, this peak appears at A_f + 365 K. This suggests an increase in the thermal stability of the B2-phase compared to the quenched state. Increasing the aging time to 4 h leads to the complete disappearance of this DSC peak (Fig. 2(b)).

After aging for 15 min, no change in the size and volume fraction of the γ-phase was identified. Whereas γ′-particles coarsen to ~ 20 nm and their volume fraction increases to 50–60 % (Fig. 3), which may contribute to the strengthening of the γ-phase.

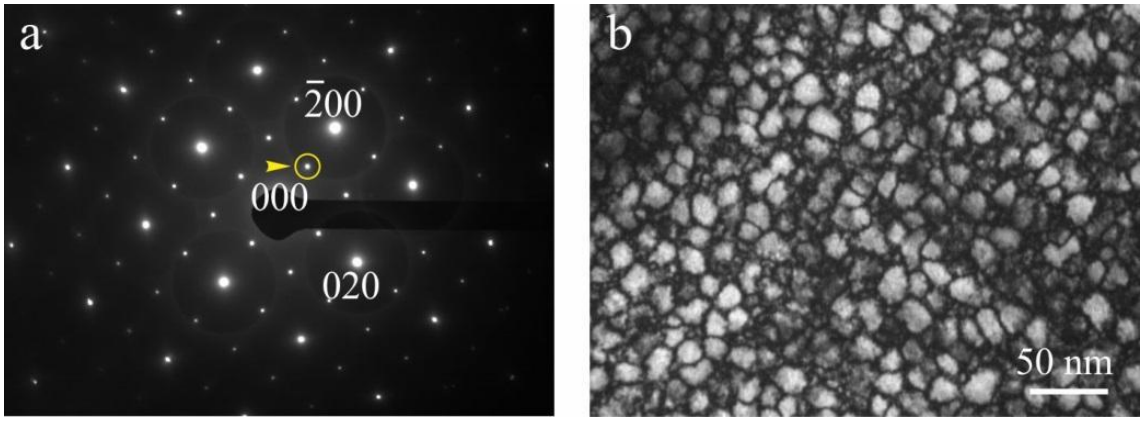


Fig. 3. TEM image of γ'-particles for aged at 673 K for 15 min $Co_{35}Ni_{35}Al_{28}Fe_2$ single crystals: (a) SAEDP from γ/γ'-phase (zone axis $[001]_{FCC}$); (b) dark-field image taken using the superlattice $(\bar{1}00)_{FCC}$ reflection (yellow arrow and circle on (a)) from nanosized γ′-particles

The endothermic peak on heating may be additionally caused by this process. An additional TEM studies are required to determine the precise evolution of γ′-particles after aging.

The enhancement of thermal stability and the significant decrease in MT temperatures just after aging are likely caused by substantial changes in the microstructure of B2-matrix undergoing the MT. After aging for 15 min, very weak additional reflections are observed in the B2-matrix, presumably associated with the presence of dispersed particles. However, no contrast from these particles is detected in dark-field images. The dispersed particles become detectable only after aging for 4 h (Fig. 4). The additional reflections (indicated by the yellow arrow and circle) from the matrix are observed and cannot be indexed within the B2-, $L1_0$-, or $L1_2$-type structures in the SAEDP. According to the dark-field analysis, these reflections correspond to the nanoscale particles with sizes ranging from 5 to 12 nm and with a high-density distribution within the B2-matrix (Fig. 4). These reflections can be reasonably indexed assuming an orthorhombic Cmmm structure corresponding to the $(Ni,Co)_5Al_3$-phase. Reflections of the (020) type and higher-order reflections are observed, indicating a reduced symmetry compared to the matrix. The orientation relationships between the $(Ni,Co)_5Al_3$-particles and the matrix are as follows: $(110)_{Ni5Al3}||(100)_{B2}$ or $[001]_{Ni5Al3}||[001]_{B2}$ [7,8,11,13]. The lattice parameters of the $(Ni,Co)_5Al_3$-particles are $a \approx 0.77$ nm, $b \approx 0.38$ nm, and $c \approx 0.66$ nm. Notably, $b \approx a_{B2}\sqrt{2}$, which explains the coherence of the $(Ni,Co)_5Al_3$-particles with the B2-matrix, resulting in insufficient contrast in dark-field images, as observed after aging for 15 min. The precipitation of secondary phase $(Ni,Co)_5Al_3$-particles leads to a local depletion of elements in the B2-matrix and reduces the MT temperatures. The decrease in the MT temperatures becomes more pronounced with prolonged aging for more 1 h, which is confirmed by $\rho(T)$ and DSC analysis.

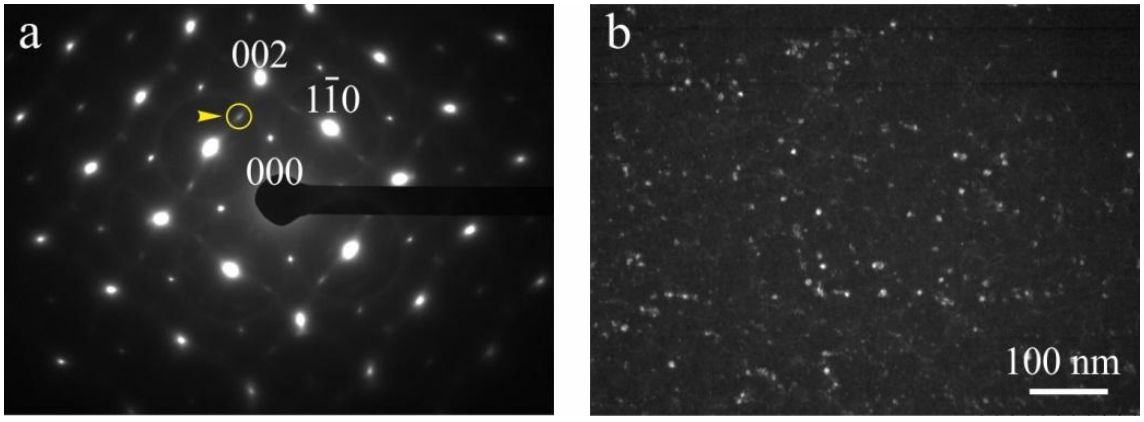


Fig. 4. TEM image of $(Ni,Co)_5Al_3$-particles for aged at 673 K for 4 h $Co_{35}Ni_{35}Al_{28}Fe_2$ single crystals: (a) SAEDP from B2-matrix and $(Ni,Co)_5Al_3$-particles (zone axis $[001]_{B2}$); (b) dark-field image taken using the reflection of the (020) type (yellow arrow and circle on (a)) from $(Ni,Co)_5Al_3$-particles

Thus, the quenched $Co_{35}Ni_{35}Al_{28}Fe_2$ single crystals are thermodynamically unstable at $T > 520$ K due to the diffusion decomposition of the supersaturated B2-phase. A decrease in MT temperatures and a reduction of the exothermic peak on DSC curves, associated with the formation of nanoscale $(Ni,Co)_5Al_3$-particles, occurs after aging at 673 K for 15 min. After aging for 4 h, this exothermic DSC peak disappears, while nanoscale $(Ni,Co)_5Al_3$-particles are detected by TEM, which suppress the thermal-induced MT.

Thermomechanical behavior during stress-induced martensitic transformation

Quenched and aged at 673 K for 15 min single crystals were loaded in compression along the [001]$_{B2}$-direction until fracture in the temperature range of stress-induced MT $T > A_f$ (Fig. 5). The $\sigma(\varepsilon)$ curves obtained at 298 and 423 K exhibit three characteristic stages associated with elastic deformation of austenite (1), the stress-induced MT (2), and elastic deformation of the stress-induced martensite (3). With increasing test temperature, stage 1 becomes longer, while stages 2 and 3 become shorter.

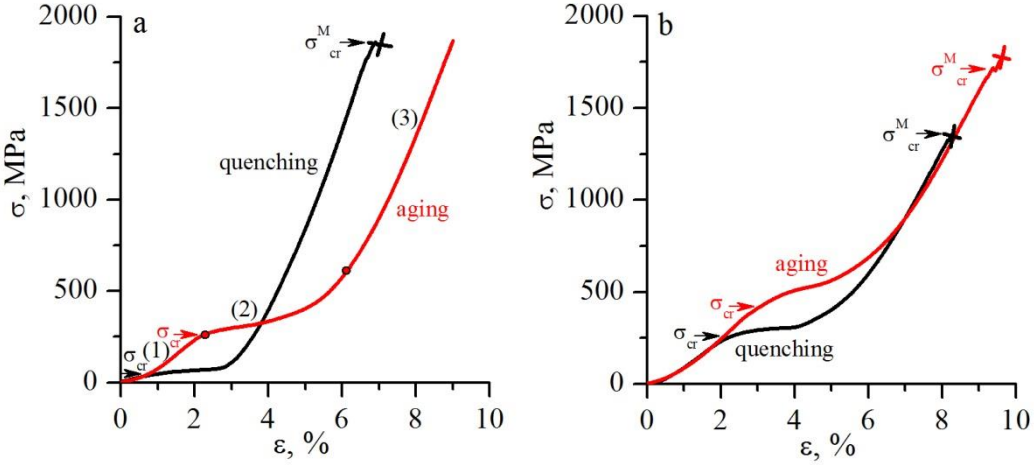


Fig. 5. $\sigma(\varepsilon)$ curves in compression along the [001]$_{B2}$-direction for $Co_{35}Ni_{35}Al_{28}Fe_2$ single crystals: (a) T_t = 298 K; (b) T_t = 423 K

The increase in stage 1 is related to the rise in the critical stress for martensite formation σ_{cr} with test temperature T_t. Figure 6(a) shows the temperature dependence of the critical stress for martensite formation $\sigma_{cr}(T)$ in compression along the [001]$_{B2}$-direction, plotted from the experimental $\sigma(\varepsilon)$ curves presented in Fig. 6(b). For both quenched and aged crystals, the coefficient $\alpha = d\sigma/dT$, which characterizes the linear increase in the critical stress for stress-induced martensite formation with temperature according to the Clausius–Clapeyron relation [25], is nearly the same and equals to 2.0 and 2.1 MPa/K, respectively. Aging leads to an increase in the critical stress by approximately 300 MPa and shifts the start temperature of the stress-induced B2-L1$_0$ MT to lower temperatures by ~ 140 K. This effect is associated with dispersion strengthening of the B2-matrix by nanoscale $(Ni,Co)_5Al_3$-particles.

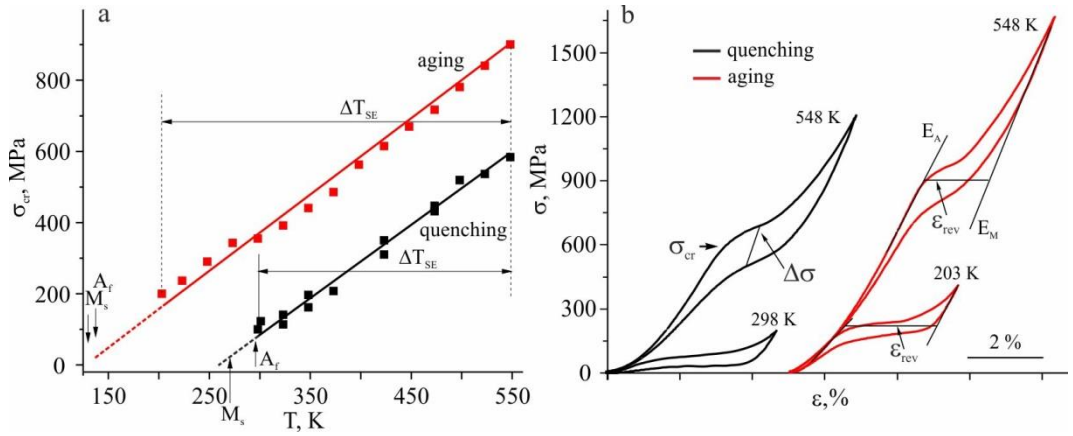


Fig. 6. Temperature dependence of stress-induced martensite formation $\sigma_{cr}(T)$ (a) and $\sigma(\varepsilon)$ curves (b) for $Co_{35}Ni_{35}Al_{28}Fe_2$ single crystals in compression along the [001]$_{B2}$-direction

In quenched $Co_{35}Ni_{35}Al_{30}$ single crystals, the temperature dependence of the critical stress for martensite formation $\sigma_{cr}(T)$ in compression along the $[001]_{B2}$-direction is nonlinear, and the coefficient $\alpha = d\sigma/dT$ increases at temperatures above 473 K. This behavior may be associated with precipitation of nanosized particles at T > 473 K [18]. In contrast, the $\sigma_{cr}(T)$ dependence is linear within the SE range in quenched $Co_{35}Ni_{35}Al_{28}Fe_2$ single crystals. Thus, the precipitation of secondary phases does not affect the stress-induced MT up to T = 520 K. As a result, Fe alloying enhances the thermodynamic stability of the B2-phase during high-temperature testing.

The reduction of stage 3 is associated with a simultaneous increase in the critical stress for stress-induced MT σ_{cr} and a decrease in the martensite yield stress σ_{cr}^{M} with increasing temperature (Fig. 5). The yield stress σ_{cr}^{M} corresponds to the plastic deformation of martensite and is equal to stress taken at 0.1 % strain (by analogy with plastic deformation by slip or twinning). The decrease in σ_{cr}^{M} with temperature is attributed to the activation of thermally activated deformation mechanisms namely the reduction of resistance to plastic deformation and increase in dislocation mobility in stress-induced martensite.

The strength properties of $L1_0$-martensite depend on the structural state. Quenched single crystals exhibit a martensite yield stress of σ_{cr}^{M} = 1860 MPa at T = 298 K, which decreases by 505 MPa with increasing temperature to 423 K (Fig. 5). These crystals fail in a brittle manner upon reaching σ_{cr}^{M}, with a maximum strain to fracture of 7.0–8.2 %. The highest strength properties are observed in aged single crystals. The yield stress of martensite exceeds 1870 MPa at 298 K without fracture (Fig. 5(a)). The strength properties of aged single crystals are σ_{cr}^{M} = 1715 MPa at 423 K, which is approximately 1.3 times higher than that of quenched crystals. The strain to fracture at 423 K in aged crystals is also higher and reaches 9.6 %.

The high strength properties of $L1_0$-martensite in compression in $Co_{35}Ni_{35}Al_{28}Fe_2$ single crystals oriented along the $[001]_{B2}$-direction is attributed to the formation of a high martensite twin density and the absence of detwinning process under stress according to loading conditions (Fig. 1(d)). The highest yield stress (σ_{cr}^{M} > 1870 MPa at room temperature) is achieved for aged single crystals due to dispersion strengthening of B2-phase by nanoscale $(Ni,Co)_5Al_3$-particles. These yield stress level surpasses the strength properties of $L1_0$-martensite in several ferromagnetic shape memory alloys in compression at room temperature, such as $(Co_{50}Ni_{20}Ga_{30})_{95}Ti_5$ polycrystalline materials (σ_{cr}^{M}≈1610 MPa) and $Ni_{54}Mn_{12}Ga_{25}Fe_9$ single crystals, oriented along the $[001]_{B2}$-direction (σ_{cr}^{M}≈1450 MPa) [26,27]. Furthermore, the yield stress level of $L1_0$-martensite for aged $Co_{35}Ni_{35}Al_{28}Fe_2$ single crystals approaches that of high-strength B19′-martensite (~ 2000 MPa) for aged at 723 K $[112]_{B2}$-oriented $Ti_{49.2}Ni_{50.8}$ single crystals, including Ti_3Ni_4-particles [28]. These results indicate that aged [001]-oriented $Co_{35}Ni_{35}Al_{28}Fe_2$ single crystals can be considered promising high-strength functional materials among SMAs.

The length of the stress plateau at stage 2 determines the reversible strain associated with the stress-induced MT. When loaded below the dislocation yield stress of martensite $\sigma < \sigma_{cr}^{M}$, the strain is fully recoverable upon unloading due to the reverse MT, i.e., the SE effect is realized (Fig. 6(b)). In quenched single crystals, a complete SE loop is observed in the temperature range from 298 to > 548 K. In contrast, a complete SE loop is realized in aged single crystals already from 203 K due to a decrease in the MT temperatures (Fig. 6(b)).

It is assumed that SE may also occur at temperatures below 203 K, since the finish temperature of reverse MT is A_f = 137 K (Table 1). Mechanical testing at temperatures below 203 K in the present study was limited by the technical capabilities of the experimental setup and requires further investigation. Nevertheless, the achieved low-temperature range down to 203 K already demonstrates the potential of this material for operation under Arctic conditions. Thus, the aging expands the SE temperature range by at least 1.4 times ΔT_{SE} = 345 K compared to quenching ΔT_{SE} = 250 K, due to the dispersion strengthening of the B2-matrix by nanoscale $(Ni,Co)_5Al_3$-particles. It should be noted that a fully reversible SE curve is observed at 548 K under high applied stresses in the loading/unloading cycle (1100 MPa for quenched and 1680 MPa for aged single crystals), indicating the high strength properties of $L1_0$-martensite at elevated temperatures (Fig. 6(b)).

Thus, the reversible strain was determined from the SE curves and is equal to the strain bounded by the tangents drawn to stage 1 during loading and to stage 3 during unloading at σ_{cr} level (Fig. 6(b)). The maximum reversible strain at SE does not depend on the structural state and equals to ε_{rev} = 3.0–3.3 % for both quenched and aged single crystals, which is consistent with similar values of the coefficient $\alpha \sim 1/\varepsilon_{rev}$. The absence of a significant change in the reversible strain and stress hysteresis ($\Delta\sigma \approx$ 115 MPa at 423 K) indicates a low volume fraction of $(Ni,Co)_5Al_3$-particles precipitated during aging for 15 min. It is also likely that the size of the nanoscale particles (5–12 nm) is smaller than the thickness of the $L1_0$-martensite twin (10–20 nm) (Figs. 1(d) and 4). As a result, the interface $(Ni,Co)_5Al_3$-particle-matrix boundary remains coherent, and the particles are inherited by the martensite. The accumulated elastic energy promotes the reverse transformation upon unloading and enhances resistance to thermomechanical fatigue.

The theoretical transformation strain for the B2-$L1_0$ MT along the $[001]_{B2}$-orientation in compression is ε_t = 4.7 %, taking into account a 10 % volume fraction of the γ-phase that does not undergo MT [22]. The reduction of the experimentally maximum reversible strain compared to the theoretical value ε_t may be associated with the formation of non-Schmid martensite variants near γ-phase boundaries during stress-induced MT.

The reversible strain decreases by a factor of 1.5–1.7 within the SE temperature range for all single crystals, leading to a reduction of stage 2 (Fig. 5 and 6(b)). Such temperature dependence of reversible strain has been previously reported for Co-Ni-Al and Ni-Fe-Ga-(Co) SMAs and is explained by the difference in the effective elastic moduli of austenite E_A and martensite E_M [29,30]. The strain determined from $\sigma(\varepsilon)$ curves depends on the critical stress for martensite formation as well as on the ratio of elastic moduli E_A and E_M, as follows:

$$\varepsilon_{rev} = \varepsilon_{tr} + \left(\frac{1}{E_M} - \frac{1}{E_A}\right) \times \sigma_{cr} \,. \quad (1)$$

As seen from the $\sigma(\varepsilon)$ curves, the effective elastic modules of austenite and martensite differ $E_A < E_M$ (Fig. 6(b)). Therefore, the second term in Eq. (1) is negative. Since the critical stress σ_{cr} increases with temperature, the magnitude of this term also increases, leading to a decrease in reversible strain. In addition, the relatively low elastic modulus of austenite indicates that, prior to stress-induced MT, the austenite lattice undergoes significant elastic distortions, and its lattice parameter reaches that of martensite. The elastic strain energy accumulated during stage 1 contributes to the thermodynamic driving force for the subsequent phase transformation and ensures the reversibility of the stress-induced MT upon unloading.

The cyclic stability of functional properties is required for practical applications of SMAs in damping devices. Figure 7 shows SE curves as a function of the cycles number *n* at a test temperature of *T* = 423 K for the studied single crystals. Thermomechanical fatigue testing was performed at a constant stress level below σ_{cr}^{M}: 600 MPa for quenched and 1100 MPa for aged single crystals. Both single crystals exhibit similar trends in the change of SE parameters with the number of cycles. The first SE cycle is characterized by the accumulation of irreversible strain of 0.3 %. In subsequent cycles from 2nd to 100th, the stress-induced MT is fully reversible and the reversible strain 2.5 % is stable. The critical stresses for martensite formation σ_{cr} decrease during the first 10 cycles by 29 MPa in quenched and by 69 MPa in aged crystals, which is accompanied by a reduction of the stress hysteresis. From 11th to 100th cycle, the critical stresses and mechanical hysteresis remain stable. Thus, SE is resistant to high-temperature cyclic testing up to *n* = 100 loading/unloading cycles for both quenched and aged single crystals.

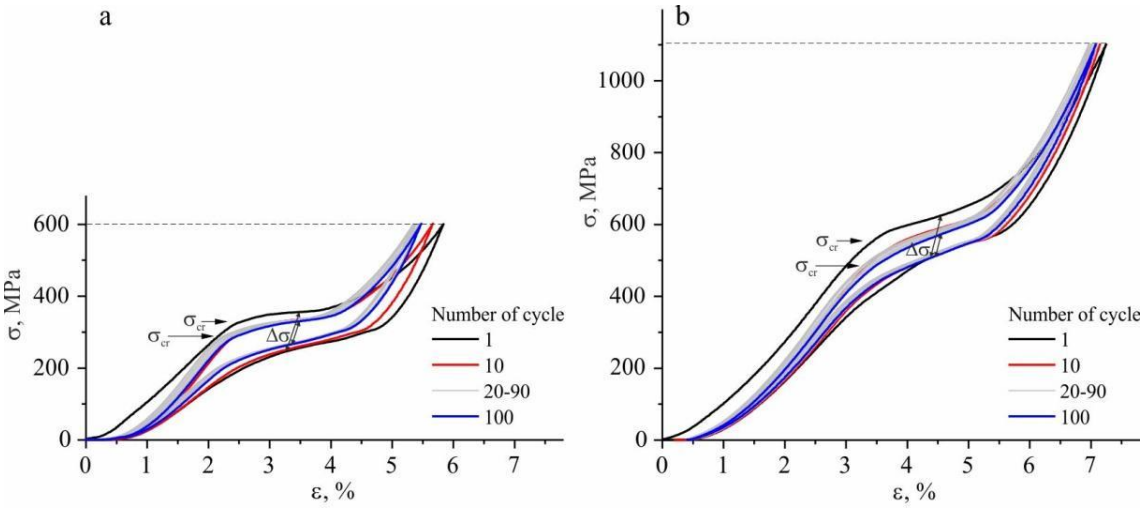


Fig. 7. *σ*(*ε*) curves as a function of the number of loading/unloading cycles at *T* = 423 K for quenched (a) and aged (b) $Co_{35}Ni_{35}Al_{28}Fe_2$ single crystals in compression along the $[001]_{B2}$-direction

The high cyclic stability of SE in $Co_{35}Ni_{35}Al_{28}Fe_2$ single crystals is attributed, firstly, to the high strength properties of $L1_0$-martensite and the large difference between the critical stress for stress-induced MT σ_{cr} and the martensite yield stress σ_{cr}^{M}. At 423 K, the critical stresses are 4.1–5.3 times lower than the martensite yield stress. Secondly, the high resistance of the high-temperature B2-phase due to a zero Schmid factor for an active $<001>_{B2}$ slip systems for the $[001]_{B2}$-orientation in compression. Thirdly, the secondary γ-phase, which contributes to the relaxation of internal stresses arising during repeated loading/unloading cycles at stress-induced MT, as previously shown for single crystals of ferromagnetic SMAs $Co_{35}Ni_{35}Al_{28}Fe_2$ [31] and Ni-Mn-Fe-(Sn) [32].

Conclusions

1. In quenched $Co_{35}Ni_{35}Al_{28}Fe_2$ single crystals, the thermal stability of the B2-phase is enhanced, and the start of diffusion processes shifts by ~ 50 K to higher temperatures up to 520 K compared to the ternary $Co_{35}Ni_{35}Al_{30}$ alloy.
2. The aging at 673 K for 15 min in $Co_{35}Ni_{35}Al_{28}Fe_2$ single crystals results in a sharp decrease in the MT temperatures by ~ 140 K, associated with the start of precipitation.

The aging for 4 h leads to the formation of nanoscale particles of 5–20 nm with an orthorhombic structure of the $(Ni,Co)_5Al_3$ type, which completely suppresses the thermal-induced MT upon cooling down to 100 K.

3. The aging at 673 K for 15 min improves the functional properties of $Co_{35}Ni_{35}Al_{28}Fe_2$ single crystals, oriented along the $[001]_{B2}$-direction in compression due to dispersion strengthening by nanoscale $(Ni,Co)_5Al_3$-particles, compared to the quenched state:

– the temperature range of SE expands by a factor of 1.4, reaching 345 K and including both low-temperature (from 203 K) and high-temperature (up to 548 K) regions;

– the strength properties of $L1_0$-martensite rise. The yield stress of $L1_0$-martensite for aged single crystals exceeds 1870 MPa at 298 K and reaches 1715 MPa at 423 K, which is about 1.3 times higher than in the quenched crystals and comparable to that of high-strength Ti-Ni-based alloys.

4. Both quenched and aged single crystals exhibit cyclic stability of high-temperature superelasticity.

CRediT authorship contribution statement

Anna S. Eftifeeva: conceptualization, funding acquisition, project administration, writing – review & editing; **Elena Y. Panchenko**: methodology, supervision, writing – review and editing; **Ilya D. Fatkullin**: investigation, visualization; **Maria V. Zherdeva**: investigation, validation; **Valentina G. Ryzhakova**: investigation, visualization; **Yuriy I. Chumlyakov**: writing – review and editing.

Conflict of interest

The authors declare that they have no conflict of interest.

References

1. Zhou F, Zhou Y, Wang Y, Liang J, Gao H, Kang M. Enlightening from γ, γ′ and β phase transformations in Al-Co-Ni alloy system: A review. *Current Opinion in Solid State and Materials Science.* 2019;23(6): 100784.

2. Kumar EK, Patel SS, Panda SK, Patle BK, Makki E, Giri J. A comprehensive exploration of shape memory alloys: Fundamentals, structural reinforcements, nano-analysis, machine learning perspective, and emerging applications. *Mechanics of Advanced Materials and Structures.* 2024;31(29): 11450–11483.

3. Oikawa K, Wulff L, Iijima T, Gejima F, Omori T, Fujita A, Fukamichi K, Kainuma R, Ishida K. Promising ferromagnetic Ni-Co-Al shape memory alloy system. *Applied Physics Letters.* 2001;79(20): 3290–3292.

4. Tian WH, Habino M, Nemoto M. Crystal structure morphology of Co precipitates in B2-ordered (Ni,Co)Al. *Intermetallics.* 1998;6(2): 121–129.

5. Bartova B, Schryvers D, Yang Z, Ignacova S, Sittner P. Microstructure and precipitates in as-cast $Co_{38}Ni_{33}Al_{29}$ shape memory alloy. *Scripta Materialia.* 2007;57(1): 37–40.

6. Bartova B, Wiese N, Schryvers D, Chapman JN, Ignacova S. Microstructure of precipitates and magnetic domain structure in an annealed $Co_{38}Ni_{33}Al_{29}$ shape memory alloy. *Acta Materialia.* 2008;56(16): 4470–4476.

7. Schryvers D, Ma Y. The growth of Ni_5Al_3 in L10-martensite studied by in situ transmission electron microscopy and high-resolution electron microscopy. *Journal of Alloys and Compounds.* 1995;221(1–2): 227–234.

8. Schryvers D, Ma Y, Toth L, Tanner L. Electron microscopy study of the formation of Ni_5Al_3 in a $Ni_{62.5}Al3_{7.5}$ B2 alloy-I. Precipitation and growth. *Acta Metallurgica et Materialia.* 1995;43(11): 4045–4056.

9. Scheerbaum N, Kraus R, Liu J, Skrotzki W, Schultz L, Gutfleisch O. Reproducibility of martensitic transformation and phase constitution in Ni-Co-Al. *Intermetallics.* 2012;20(1): 55–62.

10. Zelaya E, Esquivel MR, Schryvers D. Evolution of the phase stability of Ni-Al under low energy ball milling. *Advanced Powder Technology*. 2013;24(6): 1063–1069.
11. Muto S, Schryvers D, Merk N, Tanner LE. High-resolution electron microscopy and electron diffraction study of the displacive transformation of the Ni_2Al phase in a $Ni_{65}Al_{35}$ alloy associated with martensitic transformation. *Acta Metallurgica et Materialia*. 1993;41(8): 2377–2383.
12. Kositsyn SV, Valiullin AI, Kataeva NV, Kositsyna II. Investigation of microcrystalline NiAl-based alloys with high-temperature thermoelastic martensitic transformation: I. Resistometry of the Ni-Al and Ni-Al-X (X=Co, Si, or Cr) alloys. *Physics of Metals and Metallography*. 2006;102(4): 391–405.
13. Khadkikar PS, Locci IE, Vedula K, Michal GM. Transformation to Ni_5Al_3 in a 63.0 at. pct Ni-Al alloy. *Metallurgical and Materials Transactions A*. 1993;24A: 83–94.
14. Kataeva NV, Kositsyn SV, Valiullin AI. Formation of Ni_2Al and Ni_5Al_3 superstructures and reversibility of martensitic transformation in NiAl-based β-alloys. *Materials Science and Engineering A*. 2006;438-440: 312–314.
15. Yang JH, Wayman CM. On the Ni_5Al_3 phase and related phenomena in a NiAlFe alloy. *Materials Science and Engineering A*. 1993;160(2): 241–249.
16. Kurapova OY, Smirnov IV, Solovyeva EN, Konakov YV, Lomakina TE, Glukharev AG, Konakov VG. The intermetallic compounds formation and mechanical properties of composites in the Ni-Al system. *Materials Physics and Mechanics*. 2022;48(1): 136–146.
17. Yang JH, Wayman CM. On the formation mechanism of Ni_5Al_3 in NiAl-based alloys: Part II. Kinetics. *Intermetallics*. 1994;2(2): 121–126.
18. Eftifeeva A, Panchenko E, Chumlyakov Y, Yanushonite E, Gerstein G, Maier HJ. Compressive response of high-strength [001]-oriented single crystals of a $Co_{35}Ni_{35}Al_{30}$ shape memory alloy. *Journal of Alloys and Compounds*. 2019;787: 963–971.
19. Dadda J, Maier HJ, Karaman I, Chumlyakov YI. Cyclic deformation and austenite stabilization in $Co_{35}Ni_{35}Al_{30}$ single crystalline high-temperature shape memory alloys. *Acta Materialia*. 2009;57(20): 6123–6134.
20. Luo F-Y, Chen J-Y, Chen K-H, Oikawa K, Ishida K. Influence of Fe on martensitic and magnetic transformation of β-based CoNiAl alloy. *Journal of Functional Materials*. 2005;36(12): 1862–1865.
21. Ghasemi A, Eivani AR, Abbasi SM, Jafarian HR, Ghosh M, Mousavi Anijdan SH. Al-Co-Cr-Fe-Ni-Ti high entropy alloys: A review of microstructural and mechanical properties at elevated temperatures. *Journal of Alloys and Compounds*. 2025;1010: 178216.
22. Eftifeeva A, Panchenko E, Yanushonite E, Tagiltsev A, Ryzhakova V, Steshenko I, Chumlyakov Y. Orientation dependence of stress-induced martensite stabilization and two-way shape memory effect in CoNiAlFe single crystals. *Journal of Alloys and Compounds*. 2026;1059: 187137.
23. Yang T, Zhao YL, Luan JH, Han B, Wei J, Kai JJ, Liu CT. Nanoparticles-strengthened high-entropy alloys for cryogenic applications showing an exceptional strength-ductility synergy. *Scripta Materialia*. 2019;164: 30–35.
24. Grishchenko AI, Semenov AS, Getsov LB. Modeling inelastic deformation of single crystal superalloys with account of γ/γ' phases evolution. *Materials Physics and Mechanics*. 2015;24(4): 325–330.
25. Otsuka K, Wayman CM. *Shape Memory Materials*. Cambridge: Cambridge University Press; 1998.
26. Timofeeva EE, Panchenko EY, Dmitrienko MS, Yanushonite EI, Fatkullin ID, Chumlyakov YI. Design of NiMnGaFe alloys with high-temperature superelasticity. *Technical Physics Letters*. 2025; 51(6): 42–47.
27. Guo Z, Liu X, Xiao J, Tang L, Wang H, Zhang S, Yi X, He X. Effect of Ti doping on mechanical properties and elastocaloric effect in CoNiGa shape memory alloys. *Journal of Alloys and Compounds*. 2025;1059: 185386.
28. Sehitoglu H, Karaman I, Anderson R, Zhang X, Gall K, Maier HJ, Chumlyakov Y. Compressive response of NiTi single crystals. *Acta Materialia*. 2000;48(13): 3311–3326.
29. Li P, Karaca HE, Chumlyakov YI. Orientation dependent compression behavior of $Co_{35}Ni_{35}Al_{30}$ single crystals. *Journal of Alloys and Compounds*. 2017;718: 326–334.
30. Chumlyakov YI, Kireeva IV, Panchenko EY, Timofeeva EE, Kretinina IV, Kuts OA. Physics of thermoelastic martensitic transformation in high-strength single crystals. In: *Shape Memory Alloys: Properties, Technologies, Opportunities*. Switzerland: Trans Tech Publications; 2015. p.107–174.
31. Eftifeeva A, Fatkullin I, Tagiltsev A, Kurlevskaya I, Volochaev M, Panchenko E, Chumlyakov Y. Cyclic superelasticity behavior of $Co_{35}Ni_{35}Al_{28}Fe_2$ single crystals. *Materials Letters*. 2025; 396: 138728.
32. Li R, Liaw PK, Jiang J, Deng L, Zhang Y. Design strategy for enhancing mechanical properties and magnetocaloric effect of eutectic Ni-Mn-Sn-Fe alloy via laser powder bed fusion. *Materials Science and Engineering: A*. 2026; 954: 149795.